

Data-driven modeling of the olfactory neural codes and their dynamics in the insect antennal lobe

Eli Shlizerman · Jeffrey A. Riffell · J. Nathan Kutz

Received: date / Accepted: date

Abstract Recordings from neurons in the insects' olfactory primary processing center, the antennal lobe (AL), reveal that the AL is able to process the input from chemical receptors into distinct neural activity patterns, called olfactory neural codes. These exciting results show the importance of neural codes and their relation to perception. The next challenge is to *model the dynamics* of neural codes. In our study, we perform multichannel recordings from the projection neurons in the AL driven by different odorants. We then derive a neural network from the electrophysiological data. The network consists of lateral-inhibitory neurons and excitatory neurons, and is capable of producing unique olfactory neural codes for the tested odorants. Specifically, we (i) design a projection, an odor space, for the neural recording from the AL, which discriminates between distinct odorants trajectories (ii) characterize scent recognition, i.e., decision-making based on olfactory signals and (iii) infer the wiring of the neural circuit, the connectome of the AL. We show that the constructed model is consistent with biological observations, such as contrast enhancement and robustness to noise. The study answers a key biological question in identifying how lateral inhibitory neurons can be wired to excitatory neurons to permit robust activity patterns.

Keywords Data-driven Modeling · Reduced Dynamics · Olfactory Neural Coding · Odor Discrimination · Antennal Lobe · Contrast Enhancement · Insect Olfaction

Department of Applied Mathematics · Department of Biology · Department of Applied Mathematics at the University of Washington, Seattle, WA, USA

1 Introduction

The analysis of neural recordings from diverse sensory systems shows that meaningful sensory input is encoded into patterns of spatial-temporal activity of neuron populations. These populations, and their corresponding patterns, are termed *cell assemblies* and have been suggested to serve as the basis for the functional organization of cells for performing high-level tasks [26, 12]. The functionality of cell assemblies is substantiated by their ability to produce unique patterns of spatio-temporal activity to encode sensory information for a given modality [43, 27]. An analog for such a phenomena is an *encoding* scheme, in which the correct stimulus produces a robust, and repeatable *neural code* of spatio-temporal activity. Evidence of encoding strategies are found in different sensory systems. In olfactory and auditory systems, neural codes take the form of spatial firing-rate (FR) patterns that are exhibited by the output neurons [59, 34, 35, 53]. The spatio-temporal encoding patterns were established by the application of standard data analysis techniques, e.g., Principal Components Analysis (PCA), to the time series of FR responses of the cell assemblies [27, 8]. The success of these methods indicates that the response of cell assemblies is indeed *low-dimensional* so that for each individual stimulus a unique trajectory in a low-dimensional subspace is identified.

With these discoveries, it is intriguing to understand how sensory neural networks are designed in order to produce such behavior. Specifically, why do the encoding dynamics appear to be robust even for noisy stimuli? How is the network structure producing robust patterns of neural activity? Obtaining answers to these questions is the next challenge in unraveling the principles of sensory processing [46, 63]. For the first ques-

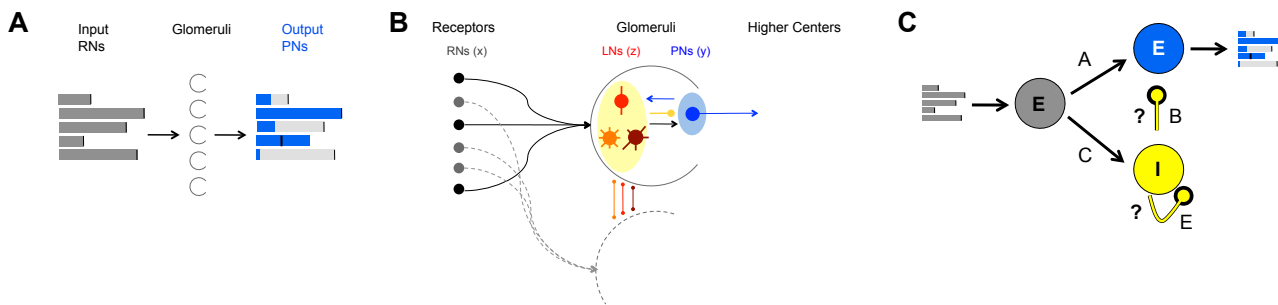


Fig. 1: AL network structure and function. (A) Demonstration of a neural code: FRs of the input neurons (gray bars) are processed by neural dynamics in the Glomeruli (half circles) in the AL and result with “shaped” FRs of the output neurons (blue bars). (B) Anatomical structure of neuron types and wiring in the AL. Both PNs (blue shaded) and LNs (yellow shaded) receive input from RNs (black balls). LNs synapse to LNs and PNs in other glomeruli via local (red), global homogeneous (orange) / heterogeneous (brown) with mainly inhibitory synapses. PNs as output neurons have excitatory synapses to neurons outside the AL, the mushroom body. (C) Schematics of a network that mimics the wiring in the AL in moths divided into three populations: input excitatory RNs (gray), interneurons inhibitory LNs (yellow) and projection excitatory PNs (blue). A,B,C and E denote the connectivity matrices between different populations of neurons, i.e., the connectome. With correct calibration of the inhibitory connections, marked by the question marks, the network can produce neural codes as in (A).

tion, investigations suggest that cell assemblies maintain several mechanisms for shaping the correct output response. One such mechanism is known to be *lateral inhibition* [34, 21], where both inhibitory and excitatory neurons receive common input and interact to mediate the response of excitatory neurons. A hallmark of lateral inhibition is an increase in the signal-to-noise ratio in encoding the input, called *contrast enhancement*. The signature of contrast enhancement is an increase in the amplitude or frequency of the response to such that it can be easily distinguished from the response to random stimuli [65, 33, 47, 19, 63]. Experimental observations of contrast enhancement show that the FR representation of the data with the right dimensionality reduction technique can potentially reveal the sensory processing mechanisms [8].

For the question of determining the network structure that is producing the robust neural codes it is necessary to model the actual network of neurons responsible for the encoding. The modeling procedure involves reconstruction of the *network wiring*, i.e., modeling individual neuron dynamics and their network interactions (*connectome*) [55, 30]. The connectome of different sensory neuronal networks may vary. For example, in vision, the retinal ganglion cells are ordered such that locally neighboring cells are responsive to neighboring parts of the visual stimulus, termed a *retinotopic map* [5]. In olfaction, output neurons are also selective for certain odorant stimuli, providing a *chemotopic map*. However, the neighboring output neurons are not necessarily similar in their tuning to specific chemicals.

Instead lateral inhibition mediates and shapes the responses of the output neurons, resulting in an *effective chemotopic map* between the input and the output cells [37, 50, 18]. Resolving this mapping is critical for determining how neurons process chemical information.

To both unravel the mechanisms responsible for the observed low-dimensional phenomena, and easily test the model for consistency with experimental dynamics, the neuronal network should be ideally modeled with a dimensionally reduced *dynamical* system. The derivation of such a system can be accomplished with two possible approaches. A bottom-up approach would model the network at the detailed synaptic level with many neurons composing a network and each neuron being a nontrivial dynamical system [10, 17]. However, the complexity of the high-dimensional system makes the extraction of a low-dimensional model challenging. Additionally, for many systems there is not enough anatomical and physiological data available to calibrate such a high-dimensional network. A top-down approach, on the other hand, would attempt to construct a low-dimensional model from the available anatomical evidence, fitting key parameters based upon experimental observations. The model can then be explored with the aim of creating similar patterns to those observed in the actual system [2, 49, 1, 38, 7]. The primary drawback of this approach is that a general framework for calibration of the model to experimental data does not exist [43, 48, 11].

To overcome this difficulty, we introduce the *dynamical dimension reduction* method that takes the top-

down approach in conjunction with experimental data. The outcome of the approach is a high-dimensional system that exhibits low-dimensional dynamics. The method is fundamentally different than the standard top-down approach, as it does not determine parameters by simulation and fitting. Instead, it projects a high-dimensional dynamical system, using *proper orthogonal decomposition*, onto orthogonal modes. It then matches the projected dynamical system with the conjectured low-dimensional dynamical system. Plugging in the experimental modes as orthogonal modes establishes the full network wiring. The constructed model can be then easily compared with the experimental dynamics for consistency. With this methodology we model the olfactory processing unit, the *antennal lobe* (AL) in the *Manduca sexta* moth, a well-characterized physiological and behavioral experimental neural system in olfaction [53, 50]. The experimental data utilized are the observed neural codes, which are an efficient representation of the measured spatio-temporal neural responses. The underlying concept of our method is that the dynamics projected onto the neural codes exhibit a trajectory towards a fixed point for each input key, a feature consistent with experimental observations. From the low-dimensional dynamics we are able to infer the network wiring for the AL. The construction of such a computational model is thereby able to answer both questions posed above since it establishes (i) a dynamical system for the FR pattern and (ii) a connectome that mimics the connectivity responsible for robust neural codes.

2 Methods and Models

2.1 Data Driven Top-Down Modeling Approach

The neural cell assemblies participating in the processing of olfactory information in the AL are the receptor cells (RNs) that carry the input from the environment, the projection (output) neurons (PNs), and local interneurons (LNs) (reviewed by [28, 25, 42]). As in the anatomical grouping, we model the network as a set of three firing-rate units corresponding to the interacting cells in the olfactory AL:

$$\dot{\mathbf{x}} = -\mathbf{x} + \mathbf{J}, \quad (1)$$

$$\dot{\mathbf{y}} = -\beta\mathbf{y} + [A\mathbf{x} - B\mathbf{z}]^+, \quad (2)$$

$$\dot{\mathbf{z}} = -\gamma\mathbf{z} + [C\mathbf{x} - E\mathbf{z}]^+. \quad (3)$$

The three groups (vectors) \mathbf{x} , \mathbf{y} and \mathbf{z} in these equations correspond to the three anatomical groups RNs, PNs and LNs respectively. The input into the PNs and LNs is modulated by a standard linear threshold function denoted by $[.]^+$, as in [37]. Figure 2A illustrates

the threshold function used here. The vector \mathbf{J} is the external input into the receptor cells which is driven by the chemosensory processes in the antenna.

In the deterministic version of this model, where the input is either constant or time dependant, the dynamics can be intuitively described. Specifically, when there is significant input into the population of receptor neurons (\mathbf{x}), these neurons lock onto the driving input \mathbf{J} [10, 11]. In the case of constant input, the receptor population will converge to a fixed point $\mathbf{x}_0 = \mathbf{J}$. This in turn excites both the projection neurons (\mathbf{y}) and the interneuron populations (\mathbf{z}). A *meaningful* input should excite a spatial *stable* pattern \mathbf{y}^P in the projection neurons. Here, the stable spatial patterns \mathbf{y}^P are thought of as library elements which distinguish (encode) various recognized odorants. Note that the pattern is not necessarily equal to the input, i.e., $\mathbf{y}^P \neq \mathbf{J}$.

Our goal is to understand how the network in Eqs. (1-3) can be made capable to produce stable patterns and discriminate between them. Particularly, we would like to find a network connectome, consisting of the connectivity matrices A, B, C , and E , that enhances the components in the input that correspond to recognized patterns (\mathbf{y}^P) and inhibit other remaining components. In practice, the structure of the connectivity matrices A and C is local and can be obtained from anatomical experimental knowledge, while the structure of the matrices B and E is mostly unknown.

The method *dynamical dimension reduction* that we introduce in this work provides a procedure to construct the unknown matrices B and E . The first step in the method is to obtain population encoding vectors (orthogonal patterns \mathbf{y}^P) from the electrophysiological recordings of PN neurons. We then show that a projection of the PN dynamical equations, Eq. (2), onto the population encoding vectors provides a division of these equations into two models: a reduced model for the dynamics of population vectors and a model for the dynamics of remaining patterns. Separating the system into two models allows us to impose constraints on the dynamics of each model. Particularly, we require stable patterns in the reduced model and rapid decay of the remainder. We show that these requirements form a convex minimization problem which solution is the unknown connectome.

The projection is done as follows. If the system does not saturate, then the excitable regime can be modeled by a linear version of Eqs. (2)-(3) in which the brackets from the saturation terms are removed. Additionally, if the \mathbf{x} dynamics are fast in comparison to those of \mathbf{y} and \mathbf{z} (RNs drive the response in LNs and PNs), then \mathbf{x} can be replaced by the input \mathbf{J} , i.e. its fixed point, and we

derive the following system

$$\frac{d\mathbf{y}}{dt} = -\beta\mathbf{y} + A\mathbf{J} - B\mathbf{z}, \quad (4)$$

$$\frac{d\mathbf{z}}{dt} = -\gamma\mathbf{z} + C\mathbf{J} - E\mathbf{z}. \quad (5)$$

In this system, the vector $\mathbf{y}(t)$ describes the dynamics of the coefficients of a standard basis ($y_i(t)$ is the dynamics of i -th PN neuron). However, we are interested in determining the dynamics of the observed patterns. From this representation, it is not immediately clear how to conclude that coding patterns in \mathbf{y} appear while others do not, and what kind of connectivity matrices support such formations. Thus the next step in our analysis is to decompose the system into the encoding patterns and a remainder. For such a decomposition, we assume that there is a library matrix L of observed patterns $L = \{\mathbf{y}_1^P, \dots, \mathbf{y}_l^P\}$. We take into account that the library is a semi-positive matrix and we normalize each column vector (pattern) in the matrix. We then transform the matrix to an *orthonormal matrix* O^P . In this matrix, each column vector is called a *population encoding vector* and represents neurons and their expected firing-rates evoked by a particular input-key. The transformation to the orthonormal matrix is achieved by applying a threshold and a maximum rule on each element l_{ij} of the matrix L . Thereby each element o_{ij}^P in the matrix O^P is defined as follows

$$o_{ij}^P = U_1(l_{ij}) = \begin{cases} l_{ij} & \text{if } l_{ij} = \max(\mathbf{l}_i) \geq \tau. \\ 0 & \text{otherwise} \end{cases}$$

where τ is the threshold value (chosen as $\tau = 0.07$ in Fig. 5). This construction results in a matrix with a single positive element in each row vector or a zero row vector, i.e., the system is effectively made orthogonal. The zero row vectors indicate PN neurons that do not substantially contribute to any of the patterns and thus these neurons will be considered to belong to the *remainder* vector. To construct the remainder vector, \mathbf{o}^R , we define the transformation U_2

$$\mathbf{o}^R = U_2(U_1(l_{ij})) = \begin{cases} 1 & \text{if } \max(\mathbf{l}_i) = 0 \\ 0 & \text{otherwise.} \end{cases}$$

that assigns the value of unity if the corresponding row in O^P that is a zero vector. As a final step we normalize \mathbf{o}^R and augment the matrix O^P with the vector \mathbf{o}^R to create the matrix O :

$$L = \begin{bmatrix} \vdots & \vdots \\ \mathbf{y}_1^P & \dots & \mathbf{y}_l^P \\ \vdots & \vdots \end{bmatrix}_{N \times l} \rightarrow^U O = \begin{bmatrix} \vdots & \vdots & \vdots \\ \mathbf{o}_1^P & \dots & \mathbf{o}_l^P & \mathbf{o}^R \\ \vdots & \vdots & \vdots \end{bmatrix}_{N \times l+1}.$$

This allows us to describe the dynamics of PNs with the following low rank decomposition

$$\mathbf{y}(t) = p_1(t)\mathbf{o}_1^P + \dots + p_l(t)\mathbf{o}_l^P + r(t)\mathbf{o}^R \\ = O \begin{pmatrix} p_1(t) \\ \vdots \\ p_l(t) \\ r(t) \end{pmatrix} = O\mathbf{p} \quad (6)$$

Here we multiply each of the population vectors (stationary) by a dynamical coefficient $p_j(t)$ and the remainder population vector by $r(t)$. To derive the equations for the dynamics of the coefficients $\mathbf{p}(t)$, we substitute the decomposition of Eq. (6) into Eq. (4) and multiply the equations for \mathbf{y} by the transpose matrix O^T and use the fact that for semi-orthogonal matrices $O^T O = I$. Thus

$$\frac{d\mathbf{p}}{dt} = -\beta\mathbf{p} + O^T(A\mathbf{J} - B\mathbf{z}), \quad (7)$$

$$\frac{d\mathbf{z}}{dt} = -\gamma\mathbf{z} + C\mathbf{J} - E\mathbf{z}.$$

This projection technique is based on the Proper Orthogonal Decomposition method introduced in [57, 58] and applied to reduction of neuronal networks in [56].

In this section we consider the case where the input is time-independent and in the Results section explore the system dynamics with time dependent and noisy inputs. Since the dynamics in \mathbf{z} are independent of the dynamics in \mathbf{p} , we can solve the second equation in Eqs. (7) for a fixed point ($d\mathbf{z}/dt = 0$)

$$\mathbf{z}_0 = \tilde{E}^{-1}C\mathbf{J}, \quad \tilde{E} = E + \gamma I.$$

Assuming that the dynamics of LNs are faster than of PNs, since LNs typically respond with bursting and release fast GABA-A transmitters (within 1-2 ms) [16], we can plug the expression of the fixed point into the first equation

$$\frac{d\mathbf{p}}{dt} = \tilde{M}\mathbf{p} + \mathbf{J}^{eff} \quad (8)$$

$$\tilde{M} = -\beta I, \quad \mathbf{J}^{eff} = O^T(A - B\tilde{E}^{-1}C)\mathbf{J}.$$

The resulting reduced system is a linear nonhomogeneous system of ODEs. It has terms that include the parameter \mathbf{p} (multiplied by \tilde{M}) and nonhomogeneous terms that are the effective input. Note that since there is no input from \mathbf{y} into \mathbf{z} in Eqs. (4)-(5), the homogeneous term is multiplied by a diagonal matrix \tilde{M} . The matrix \tilde{M} has only negative eigenvalues ($\lambda_i = -\beta$) and thus by Lyapunov's stability theorem the model in Eq. (8) is globally asymptotically stable, i.e the system will always converge to a stable equilibrium $\mathbf{p}_0 = (1/\beta)\mathbf{J}^{eff}$ [23], see Fig. 2C. In systems which have additional input from the \mathbf{y} population into the \mathbf{z} population, the matrix \tilde{M} will involve non-diagonal terms that

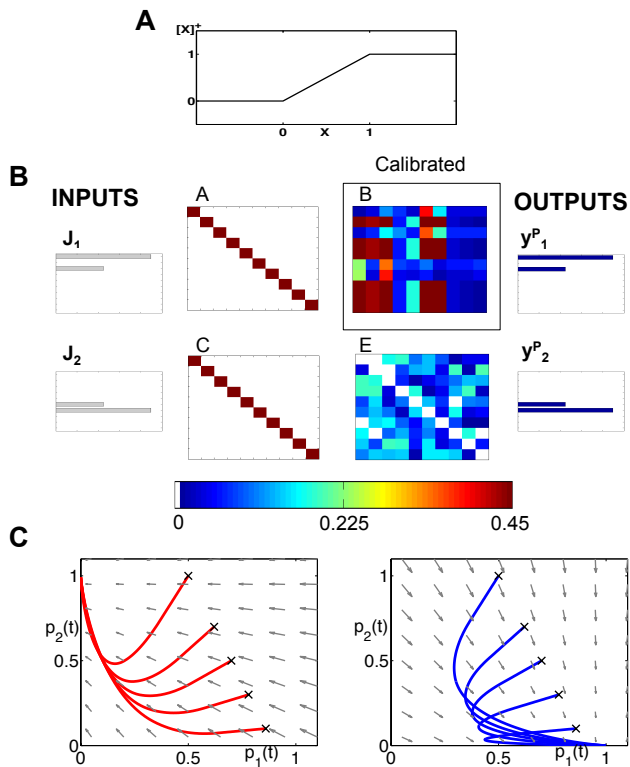


Fig. 2: **Modeling approach to the dynamics of the AL.** (A) Piecewise linear f-I curve that we use to model the neurons as FR units. (B) Example of a calibration of a network, consisting of ten neurons from each class and encodes two neural codes. The input keys $\mathbf{J}_1, \mathbf{J}_2$, and the population vectors $\mathbf{y}_1^P, \mathbf{y}_2^P$ with given connectivity matrices A, C, E allow us to reconstruct the matrix B .

We use the matrix $W = \begin{bmatrix} 1 & -0.4 & 0 \\ -0.4 & 1 & 0 \\ -1 & -1 & 1 \end{bmatrix}$ to prescribe the low-dimensional projected system. (C) Deterministic dynamics when the input is the key: \mathbf{J}_1 (left) or \mathbf{J}_2 (right). When \mathbf{J}_1 is applied, the fixed point is located at $(p_1, p_2) = (1, 0)$ and all trajectories are attracted to it (see blue sample trajectories with initial conditions denoted by 'x'). When \mathbf{J}_2 input is applied, the trajectories are being attracted to $(p_1, p_2) = (0, 1)$ (see red trajectories).

express interactions of the patterns. For such wirings it should be verified that the system is stable, i.e. the dynamics are as in Fig. 2C, by solving the Lyapunov equation that will involve the connectivity matrices [23]. The solution of the equation, if exists, will impose constraints on the configuration of the connectivity matrices such that the fixed point is stable. These constraints will be added to the optimization problem 11.

While the stability theorem assures that the dynamics of the patterns converge to an equilibrium, it does not guarantee separation of equilibria, which is required for a robust encoding-decoding system. Moreover, the matrices B and \tilde{E} are unknown, both in theory and in practice. For that purpose we need to calibrate the effective input into the population encoding vectors. Following the same procedure as for the output patterns we construct an *orthogonal library matrix*, J_0 , for the input keys. Then the calibration is reduced to solving the following system of underdetermined equations

$$O^T(A - B\tilde{E}^{-1}C)J_0 = W. \quad (9)$$

with the prescribed matrix W of dimensions $(l+1) \times (l+1)$ representing the calibration, and B and \tilde{E} are the unknown matrices. Essentially, this is a linear system of equations with a specified right hand side matrix W where the matrix elements of W determine physiologically relevant characterization of the importance of various odors. This is a highly underdetermined set of equations that allows for an infinite number of solutions, i.e. there are an infinite number of ways to specify B and E . Thus further constraints must be imposed in order to arrive at a biophysically valid solution.

Each row in W encodes the effect of the different input keys, including the remainder, on a particular population encoding vector. For example, the element on the i -th row and k -th column, $w_{i,k}$, defines how \mathbf{J}_k excites or inhibits $p_i(t)$. The elements of W are set as follows

$$W = \begin{bmatrix} \cdot & \cdot & \cdot \\ \cdot & w_{i,i} & w_{i,k} & w_{i,l+1} \\ \cdot & \cdot & \cdot & \cdot \\ w_{l+1,1} & w_{l+1,k} & w_{l+1,l+1} \end{bmatrix}. \quad (10)$$

The diagonal element on the i -th row, $w_{i,i}$, defines how \mathbf{J}_i affects $p_i(t)$, its corresponding population encoding vector, and has to be set as positive (excitatory). The input from the other keys, $\mathbf{J}_k, k \neq i$, is encoded by $w_{i,k}$ and can be set 0 or negative. The input from the last key is the input from the remainder and is encoded by $w_{i,l+1}$. The value of this element should be strictly set to 0, such that the remainder does not have excitatory or inhibitory effect on the population encoding vector. The last row in W denotes the input into the remainder and thereby the elements, except the diagonal element on that row should be always negative. See the caption of Fig. 2 for a possible configuration of the matrix W .

When A and C are known matrices, then the calibration is accomplished by solving an inverse problem to find the matrices \tilde{E} and B that satisfy these equations. Notice that the equations are underdetermined, i.e., the dimensions of W are much lower than

of $B\tilde{E}^{-1}$, indicating that the matrices B and \tilde{E} that satisfy Eq. (9) are non-unique. To find the appropriate candidates for the matrices, we reformulate the inverse problem as a convex minimization problem

$$\begin{aligned} \text{minimize } & \|O^T(A - B\tilde{E}^{-1}C)J_0 - W\|_{Fr} \\ \text{subject to } & B, E \geq 0, \end{aligned} \quad (11)$$

where $\|\cdot\|$ is the Frobenius matrix norm. When the lateral connections between PNs and LNs are exclusively inhibitory the matrices B, \tilde{E} are non-negative. When one of the matrices is set to particular wiring (e.g. \tilde{E} is random) we need to determine only one matrix and the minimization problem is a semi-definite convex minimization. When there are excitatory lateral connections or the zero minimum cannot be attained, the semi-definite constraint is relaxed. Another possibility for negative terms in B and \tilde{E} is when the input keys and the output codes differ from each other in dimensions. Indeed, the matrices B and \tilde{E} permute the lateral effect of the interneurons to support such a coding scheme. Due to many degrees of freedom in the problem, additional constraints can be added. For example we can restrict the magnitudes of the elements in B and \tilde{E} not to exceed a particular value. Moreover, the calibration is particular to the choice of the matrices A and C (see an example in Fig. 2B). To solve the minimization problem (11) or its variants, we employ the disciplined convex optimization package CVX implemented in MATLAB [24].

For input keys being identical to the output population vectors, i.e. $J_0 \equiv O$, the calibration creates a system that for a significant magnitude of one of the input keys, noise and other population encoding vectors will be suppressed to allow for a decoding of the input-key (see Fig. 4). Effectively this is a mechanism that produces contrast enhancement as we discuss in the Results section.

2.2 Electrophysiological preparation and stimulation

Manduca sexta L. (Lepidoptera: Sphingidae) larvae were obtained from the *Manduca*-rearing facility of the Department of Biology of the University of Washington. Larvae were reared on artificial diet [3] under long-day light:dark (LD) regimen (LD 17:7) at 25-26 °C and 40–50% relative humidity (RH), and prepared for experiments 2-3 d after emergence. In preparation for electrophysiological recording, the moth was secured in a plastic tube with dental wax, leaving the head and antennae exposed. The preparation was oriented so that both ALs faced upward, and the tracheae and sheath overlying one AL were carefully removed with a pair of

fine forceps. The brain was superfused slowly with physiological saline solution throughout the experiment.

Electrophysiological recordings were made with 16-channel silicon multielectrode recording arrays (a4×4–3mm50–177; NeuroNexus Technologies, Ann Arbor, MI, USA). This microprobe allows the recording of neurons throughout the AL because of the probes dimensions, with four shanks spaced 125 μm apart, each with four recording sites 50 μm apart [15, 54]. The probe was positioned under visual control using a stereo microscope. We use routine histological methods (e.g., Riffell et al. [53]) to visualize the tracks left by the probes and identify the recording sites. Neural ensemble activity was recorded simultaneously from the 16 channels of the recording array using a RZ2 base station (Tucker-Davis Technologies, Alachua, FL USA) and a PZ2 peamplifier. Spiking data from 16 channels (recorded at four sites on each of the 4 probes) were extracted from the recorded signals and digitized at 25 kHz using the Tucker-Davis Technologies data-acquisition software. Spike data were extracted from the recorded signals in the tetrode configuration and digitized at 25 kHz per channel. Filter settings (typically 0.6–3 kHz) and system gains (typically 5,000–20,000) were software adjustable on each channel. Spikes were sorted using a clustering algorithm based on the method of principal components (PCs). Only those clusters that were separated in three dimensional space (PC1–PC3) after statistical verification (multivariate ANOVA; $P < 0.05$) were used for further analysis (6–15 units were isolated per ensemble; $n = 11$ ensembles in as many animals). Each spike in each cluster was time-stamped, and these data were used to create raster plots and to calculate the instantaneous firing-rates (iFRs). Based on the spiking activity, recorded spike trains were identified as an LN or PN (as in [36, 53, 9, 52]). All analyses were performed with Neuroexplorer (Nex Technologies, Winston-Salem, NC, USA), or MATLAB (The Mathworks, Natick, MA, USA), using a bin width of 5 ms, unless noted otherwise.

Olfactory stimuli were delivered to the preparation by pulses of air from a constant air stream were diverted through a glass syringe containing a piece of filter paper bearing floral odors. The stimulus was pulsed by means of a solenoid-activated valve controlled by the acquisition software (Tucker-Davis Technologies, Alachua, FL USA). AL neurons were stimulated with two odorants: β -myrcene, a plant-derived odorant used to attract moths [53]; and E10,Z12-hexadecadienal (bombykal {Bal}), the primary component of the conspecific females sex pheromone [60, 61]. Stimulus duration was 200 ms, and five pulses were separated by a 10 s interval. The stimulus durations reflect the time periods in which moths

encounter odors when flying in their natural environment [45,51], and the odorants used to stimulate the preparation are behaviorally effective stimuli, thus allowing neurobiological experimentation in a naturalistic context for discovering how neural circuits process odor information.

3 Results

To study the AL’s neural encoding dynamics we computationally model the AL as a network with each neuron modeled as a FR unit. In keeping with the populations of AL cells, three populations of FR units are considered: receptor cells that carry the input from the periphery (RNs), projection (output) neurons (PNs), and local inhibitory interneurons (LNs) (Fig. 1). The dynamics of the populations are represented by the state vectors, \mathbf{x} , \mathbf{y} and \mathbf{z} corresponding to dynamics of RNs, PNs and LNs respectively. Each FR unit in each population is modeled by a differential equation that describes unit’s self-dynamics (decay in the absence of input), interaction with other units and response to odorant stimulus (for a detailed description of the construction see the Methods section). The network can be calibrated to perform encoding functions, i.e., produce neural codes. Specifically, for each FR pattern that the PNs population exhibits (called *population encoding vector*), there is a FR pattern of the RNs population that evokes it (called *input key*) (depicted in Figs. 1,2). The results that we obtain from constructing the network establish how neurons’ connectivity and network dynamics are linked together to produce these encoding functions. Analyzing computational dynamics and comparing them with experimental dynamics elucidates what are the typical dynamics of neural codes and how they can be perceived. We describe our results in detail below.

3.1 Recovering the Connectome of an Example Network

As an illustrative example of the theoretical construct proposed here, we demonstrate how we establish the neuronal wiring on a network of 10 neurons of each type: 10 RNs, 10 PNs and 10 LNs for a total of 30 neurons. The network is designed to encode two input keys into two output population encoding vectors (codes) identical to the input keys. The goal of the calibration is to determine the connectivity matrix B given the matrices A , C and E (Fig. 1C). Specifically, we choose the matrices A and C to be identity matrices, i.e., each receptor is connected to its corresponding PN and LN.

The matrix E is set as a random matrix whose elements are drawn from a uniform distribution with mean 0.25, i.e., the LNs are randomly connected between themselves. We then solve an optimization problem, Eq. (11), derived in the Methods section, to determine the elements of the matrix B . This is the optimal matrix that supports such an input-output relation (Fig. 2B). The matrices are asymmetric, showing that our approach is consistent with experimental anatomical data. Moreover, it is fundamentally different than the Hopfield-type approach that uses symmetry constraint for optimization [50, 29].

The calibration process produces connectivity matrices from which the connectome of the full network is recovered. To visualize the connectome we use the CIRCOS package [32] (Fig. 3A) where the network is depicted in a ring shape: FR units are drawn as arcs on the ring’s perimeter and the connections are the links between the arcs. The connectome structure allows us to observe that indeed the remainder PNs, labeled as ($y_2, y_4 - y_6, y_9, y_{10}$), have stronger input inhibitory connections (dark bold red curves) than the PNs that participate in the output codes, labeled as (y_1, y_3, y_6, y_7). We further observe that these strong connections are output connections of LNs, activated by RNs participating in one of the keys, labeled as (x_1, x_3, x_6, x_7). This confirms that the strong inhibition of the remainder PNs is activated only when there is enough input from RNs participating in the keys. In addition, each input key activates the suppression of the other key, though less strongly than the suppression of the remainder. This is expected from the calibration matrix W specification (see caption of Fig. 2, and the definition of W in Eq. (10). The random connections between the LNs, defined by the connectivity matrix E , are seen in the graph as edges marked by light red color.

Once the connections are determined, the deterministic dynamics of the calibrated connectome defined in Eqs. (1)-(3) can be explored computationally in order to verify that the calibration gives the desired low-dimensional dynamics. In Fig. 3B,C we depict the *active pathways* in the connectome, i.e., the pathways activated by the input keys. We demonstrate that for the input \mathbf{J}_1 (Fig. 3B) four excitatory edges are activated in the connectome, where the edges from x_1 are stronger than from x_3 as expected. These edges excite LNs that activate inhibitory pathways to PNs. The strongest inhibitory pathway is invoked by z_1 that suppresses strongly all remainder PNs. There is also relatively strong suppression of the PNs that participate in the input key \mathbf{J}_2 and very weak suppression of PNs that should be activated when the input is \mathbf{J}_1 . For the

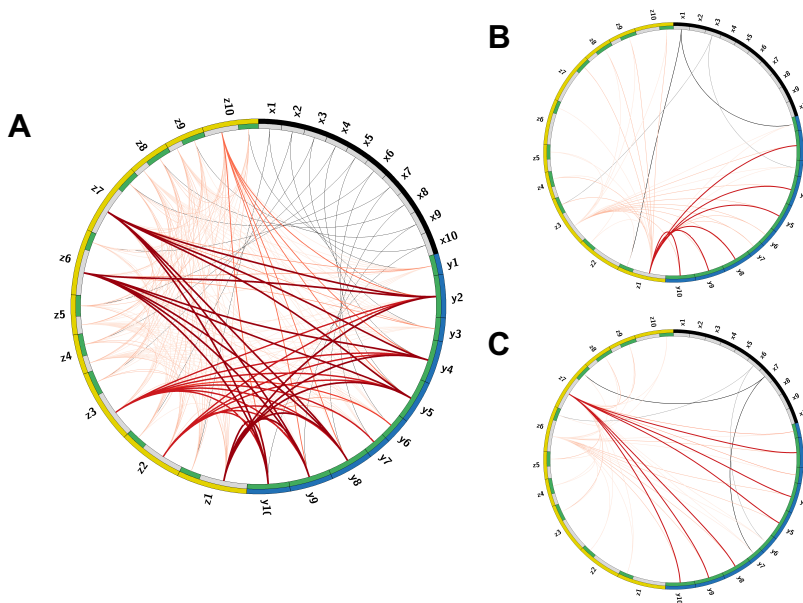


Fig. 3: **Visualization of the Connectome.** (A) The connectome (neurons and their connections) of the reconstructed network depicted in a ring shape. The nodes on the outer ring correspond to RNs, LNs and PNs and marked by black, yellow and blue colors respectively. The inner ring splits each node into “in” and “out” terminals colored by gray and green colors. The edges denote connections between the nodes. Excitatory connections are displayed by gray color and inhibitory by red color. The shades and width of the edges denote the strength of the connections (darker and wider curve corresponds to a stronger connection). (B,C) Activated pathways in the connectome when the input is the key: \mathbf{J}_1 (B) or \mathbf{J}_2 (C). The shades and width of the “out” edges in the connectome scaled by the input into the node. When there is no input into the node, its “out” edge is not shown.

input key \mathbf{J}_2 (Fig. 3C) the remainder is strongly suppressed again, but by a different LN ($z7$). Moreover, the suppression of neurons that should respond to \mathbf{J}_1 is stronger than that of \mathbf{J}_2 , i.e. the suppression is switched as expected to support \mathbf{J}_2 instead of \mathbf{J}_1 .

From the structure of the effective connectome, we can conclude that it indeed produces the expected *low-dimensional* dynamics. Further verification is shown in Fig. 2C where the dynamics of the full network are exactly the dynamics of the prescribed low dimensional system, Eq. (7). When \mathbf{J}_1 is the input, Fig. 2C (left), all trajectories are attracted to a unique stable fixed point on the vertical axis, and when the input is \mathbf{J}_2 , Fig. 2C (right), the trajectory is attracted to the unique stable fixed point on the horizontal axis.

3.2 Noisy Inputs

Input into the AL varies significantly as a function of time due to environmental effects, thus producing low signal-to-noise ratio input signals to the AL. We can use the example network as a prototype system to study the stochastic dynamics of such networks and the im-

plications on the calibration proposed here. To simulate noisy inputs, we define the input as $\mathbf{J} = \alpha \mathbf{J}_k + \sigma \eta(t)$ and define the signal-to-noise ratio (SNR) as α/σ . Our objective is to verify that for different SNR ratios, the performance of the network produces the correct population encoding vector. As demonstrated in experimental studies of olfaction and other sensory systems, the underlying neural networks for signal processing, e.g., the AL in olfaction, produce contrast enhancement. To quantify the contrast enhancement, we introduce the measure, contrast over time (CRT), for a noisy input key \mathbf{J}_k , defined as $CRT_k = p_k(t) - \sum_{j=1, j \neq k}^l p_j(t) - r(t)$. This describes the difference between the k -th population encoding vector, $p_k(t)$, and the summed dynamics over all other population encoding vectors, $p_j(t)$, and the remainder, $r(t)$.

Intuitively, the measure will be larger when there is a better separation between the correct input and all other possible inputs. We investigate the average CRT over time vs. SNR in Fig. 4 (left) for three different network structures where the matrix B is *calibrated*, *uncalibrated* (random with different magnitudes) and has *no inhibition* (all zeros). It can be clearly observed

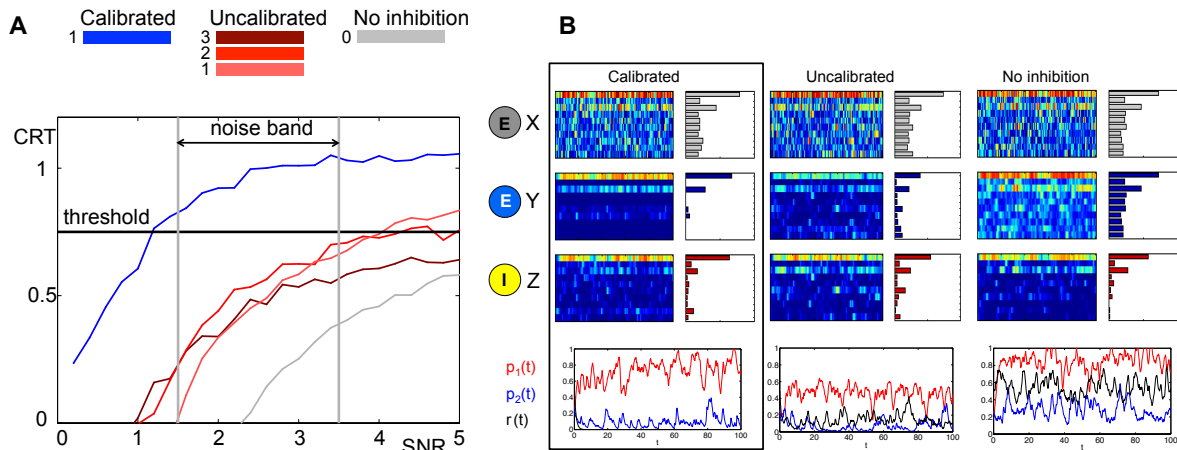


Fig. 4: **Comparison of stochastic dynamics of an example network calibrated as in Fig. 2B,C.** (A) Contrast (CRT averaged over 10 runs) vs. SNR for different choices of the connectivity matrix B : calibrated by (11) (blue), elements drawn from a random uniform distribution with $m \times 0.5$ mean: $m = 1$ (pink), $m = 2$ (red) and $m = 3$ (brown), connections are blocked $B \equiv 0$ (gray). (B) Dynamics of a network with noisy input \mathbf{J}_1 (signal-to-noise ratio SNR=3) for different choices of the connectivity matrix B (from left to right): calibrated by (11), elements drawn from random uniform distribution with mean 0.5, connections are blocked $B \equiv 0$. The elements of the matrix E are drawn once from a uniform distribution and fixed. The color raster plots show the FR dynamics of the neurons in X (RNs), Y (PNs) and Z (LNs) classes (blue:low FR, red:high FR). The bar plots on the right side of each raster plot show the average FRs over the whole evolution. The bottom plots show the projection of Y neurons onto the patterns \mathbf{o}_1^P , \mathbf{o}_2^P and \mathbf{o}^R corresponding to $p_1(t)$, $p_2(t)$ and $r(t)$ and depicted with red, blue and black colors respectively.

that the calibrated network achieves the best CRT out of all other network wirings. The calibrated network exhibits a 1.5 – 4 fold increase in CRT values in comparison to its corresponding uncalibrated networks, and a 10-fold increase over the case where there is no inhibition. In particular, network calibration is important at low SNR ratios (1.5 to 3.5), which is the expected noise band in the actual environment [4, 51, 54]. Otherwise, the correct population encoding vector cannot be separated from the background noise, Fig. 4A. Indeed, only the calibrated CRT curve is able to cross the 0.75 CRT threshold (approximately 75% of separation) in that SNR band. By varying the amplitude of the uncalibrated connections we illustrate that the amplitude of the elements in B do not necessarily improve the CRT. When the amplitude is low (see gray curve for 0 amplitude) the performance is poor because the activity is noisy. Incrementally increasing the amplitude improves the performance such that it is able to cross the CRT threshold when SNR exceeds 4 (red curves). However, for a calibrated network the crossing of the threshold happens for much lower values of SNR. Remarkably, even for SNR lower than 1 (where noise prevails over the signal) the calibrated CRT curve (blue) is already crossing the threshold. Additional increase in the amplitude of the inhibitory connections will inhibit both

noise and the signal, and we indeed observe that the CRT curve (brown) drops lower than the lowest amplitude curves and does not cross threshold in the 0-5 SNR band.

To understand the contrast enhancement more intuitively, we show in Fig. 4B the dynamics for SNR=3. At this SNR, the dynamics of RNs and LNs are very similar for all network wirings. The dynamics of RNs are noisy, making it very difficult to recover the input key from the data. The dynamics of LNs are cleaner, but still do not have a clear signature of the input key signal. In particular the ratio between the two elements of the key, neurons 1 and 3, is incorrect. The dynamics of the PNs, however, are very different for the three choices of network wirings. In the calibrated network the dynamics of PNs are more distinguishable relative to other networks. Indeed, both FRs over time and average FRs indicate that the output signal is the closest to the population encoding vector \mathbf{o}_1^P corresponding to the input key \mathbf{J}_1 (the CRT value is around 1). For uncalibrated or no lateral inhibition wirings, such a clear signature cannot be detected. Indeed the CRT measure for uncalibrated network is 0.55 and for no inhibition network is 0.2. These dynamics reflect the underlying network structure. Thus for the uncalibrated network, all population encoding vectors are being inhibited pro-

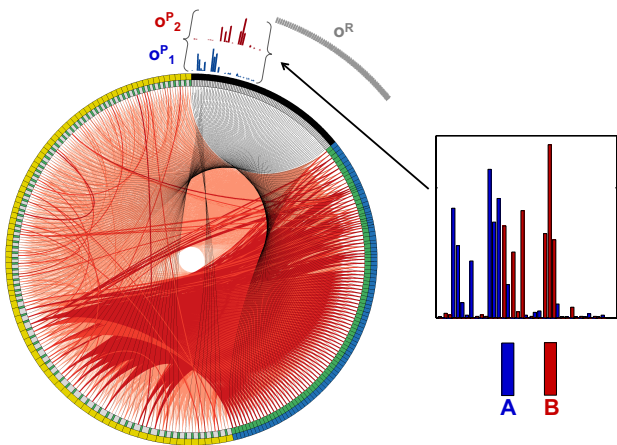


Fig. 5: Library elements and the reconstructed connectome produced from experimental data.

The connectome of a network of 97 neurons of each type (291 in total), obtained from solving the minimization problem in (11) with the matrices A, C chosen as identity matrices and E as a positive random matrix with elements drawn from a normal distribution, i.e., $e_{ij} \sim |N(0, 0.02)|$. The connectome is visualized in a ring shape with similar choice of colors as in Fig. 3A. The orthogonal library matrix, O , used in the minimization, was obtained from the electrophysiologically recorded data of two odorants A and B as described in §§Construction of the Data-Driven Model in Results. The three library vectors \mathbf{o}_1^P , \mathbf{o}_2^P and \mathbf{o}^R in O , correspond to the odorants A (blue), B (red) and the remainder (gray) respectively, are depicted as bar-plots above the connectome at the locations that correspond to RNs that evoke each of the vectors. To the right of the connectome, the bar-plots of the vectors \mathbf{o}_1^P and \mathbf{o}_2^P are enlarged. The threshold value, τ , used to construct the library vectors, is $\tau = 0.07$.

portionally so that detection of the correct output both from the averaged FRs histogram and/or the projected dynamics is more difficult. Similar behavior, but even more noisy, occurs when there is no lateral inhibition.

We also compared the calibrated and uncalibrated wirings obtained from data (stimuli C and D) by adding noise of $\sigma = 0.3$ (SNR=3) to the models and computing the CRT trajectory over time for each simulation (5 simulations per wiring), see Fig. Sup. 1. Indeed, the CRT trajectories produced by the calibrated model cross the correct threshold while trajectories produced by the random model do not cross it. In addition, when the stimulus is off the trajectories produced by randomly wired model are very sensitive to noise to the extent that they can cross the wrong threshold.

3.3 Construction of the Data-Driven Model

We proceed and construct a dynamical model using the experimental data. In the first series of experiments we recorded from 130 PNs that were stimulated with two odorants: “A” (BAL-Bombykal), “B” (MYR- β -Myrcene). These stimuli are behaviorally effective odorants: odorant A is a component of the moth sex pheromone, and odorant B is a flower scent component. These odorants excite distinct glomeruli in the AL and require a minimal orthogonalization of the library. Therefore, we chose them to validate the data-driven model construction part of our approach. Another reason for the choice is that they are (negatively) correlated with each other – when a particular stimulus is on, PNs associated with it are excited while those associated with the other stimulus are inhibited (see Fig 1 Sup). This suggests that these regions inhibit each other via lateral inhibition. We also recorded from 70 PNs with two related stimuli: “C” (BEA-benzaldehyde), “D” (BOL-benzyl alcohol) that excite PNs in overlapping glomeruli. Both odorants are dominant in floral scents related in chemical structure as oxygenated aromatic volatiles.

The odorants are presented to the preparation at a realistic time interval (200 msec) repeatedly for five stimulations separated by long intervals of no input. For more information regarding the experimental setup and procedures see the subsection ‘Electrophysiological preparation and stimulation’ in the Methods section. The data is available in the supplementary material. With the spike trains of each PN we have computed the time series of the instantaneous FR (iFR) averaged over the 5 trials of odor introduction. Sampling the iFR at a specific time after the beginning of the odor introduction (at 150 msec) or performing a PCA reduction and taking the first dominant mode, we obtained a histogram of iFRs for the neurons for each of the odors. The neurons with substantial difference in iFR in response to the two odorants were assigned as selective neurons (37 neurons for A,B and 30 neurons for C,D). Those with low iFR were assigned as remainder neurons (60 neurons for A,B and 40 neurons for C,D). The remaining neurons that exhibited high iFR were not included in the calibration (33 neurons for A,B) since there was not enough data to calibrate the inhibitory connections to them.

Application of the orthogonalization procedure, defined in the Methods section, for the 97 neurons for A,B and 70 neurons for C,D resulted in the two population encoding vectors: \mathbf{o}_1^P for A (blue) and \mathbf{o}_2^P for B (red) as shown in Fig. 5 (vectors for C,D are similar so were not shown). For A,B the required orthogonalization is

minimal, while for C,D it is significant as shown in Fig 2 Sup.

This allows for the reconstruction of the *connectome* of the AL network in a similar fashion to the example network. Here the matrix E is taken as a random normal matrix and the matrix B is calibrated. The full network consists of the three populations (PNs, LNs, RNs) of 97 neurons (291 neurons in total), where in each population we depict (in the clockwise direction) the selective neurons followed by the remainder neurons (Fig. 5). Although many connections exist, the ring shaped visualization demonstrates qualitatively the main features of the connectome: (i) the suppression of the selective neurons seems to be nonuniform and sparse while (ii) the inhibition of remainder neurons is uniform and dense. These biophysical wirings are consistent with the derived population encoding vectors that are nonuniform.

3.4 The Dynamics of Population Encoding Vectors

The orthogonality of the population encoding vectors, \mathbf{o}_1^P and \mathbf{o}_2^P , allows us to construct a two dimensional space, called the *odor space*. We use it to project the iFR time series obtained from either the data or the calibrated model. The data projection is used to assess whether the experimental dynamics are consistent with the underlying dynamical mechanism in the construction of the model. Specifically, there is a single, stable fixed point in each encoding vector direction. Figure 6 shows the projection dynamics (gray) of five experimental trials along with the average trajectory over the trials (black). Before the input is applied, the projected trajectory hovers around vicinity of the origin due to noise fluctuations. When the input is applied, the trajectory begins an excursion toward the stable fixed point and when the input is off, the trajectory returns to within the vicinity of the origin. The input of odor ‘‘A’’, ‘‘C’’ corresponds to trajectories whose fixed point lies on the vertical axis while odor ‘‘B’’, ‘‘D’’ trajectories evolve trajectories towards a fixed point on the horizontal axis.

Data projections from both the experimental data and the calibrated model, Fig. 6 and supplementary videos, clearly demonstrate that different odorant inputs correspond to different orthogonal fixed points in the projection space. Furthermore, trajectories appear noisy while reaching the fixed point whereupon they remain static for a while until the input is stopped and then trajectory returns to the origin.

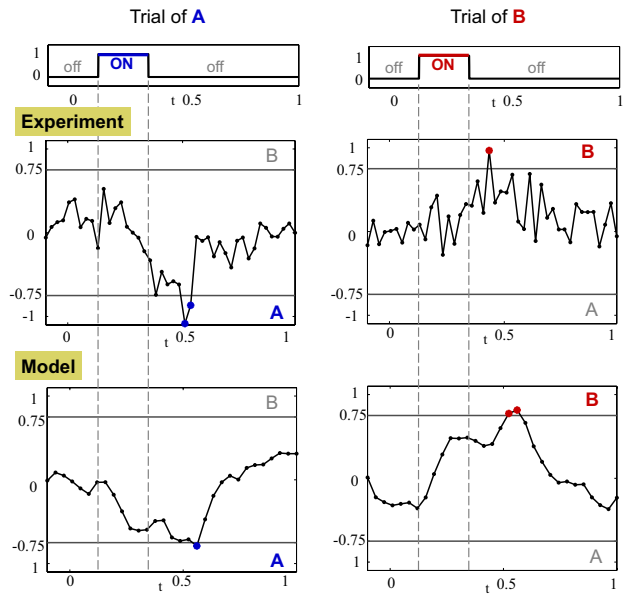


Fig. 7: **CRT dynamics demonstrates the decision making associated with odor detection.** Left and right columns show the dynamics of $CRT_{A/B}$ measure for one trial of stimulus A and B respectively. The CRT measure computed for stimuli A and B is: $CRT_{A/B} = p_B(t) - p_A(t) \pm r(t)$. Top row: the amplitude of the stimulus input over time. Middle and bottom rows: CRT dynamics, in the experiment and in the calibrated model respectively. The threshold decision lines are plotted with gray color at -0.75 (A) and 0.75 (B). When the CRT curve (black line with dots corresponding to data points) crosses the threshold, the data points are marked with appropriate color of their dots: blue for stimulus A and red for stimulus B.

3.5 Decision Making

In the experiments described here, the presentation of a stimulus odor occurs for an extremely short period of time (approximately 200 ms). Such inputs correspond to realistic stimulus for which the moth is flying and sampling odors in a turbulent environment. Thus once we have characterized the dynamics of each short trial, we aim to deduce the dynamical mechanism that corresponds to a sequence of short bursts of inputs and its benefits on odor detection and selection.

To formulate the decision making process, we analyze the dynamics of a trajectory toward the orthogonal fixed point when the stimulus is introduced as demonstrated in Fig. 6. The orthogonality of the fixed points allows us to construct *threshold lines* for determining odor detection. The gray horizontal and vertical lines in Fig. 6 represent the threshold for the detection of

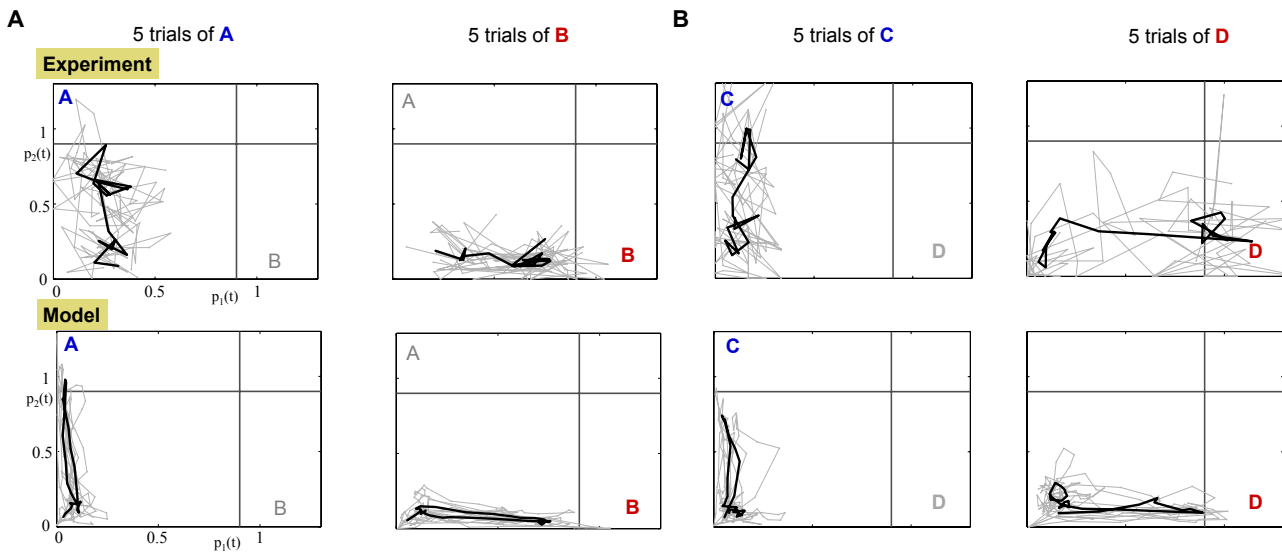


Fig. 6: **Projection of the experimental and model dynamics onto orthogonal odor space.** Top row: projected experimental dynamics of PNs. Bottom row: projected dynamics of the calibrated model. Each column shows 5 distinct trials per stimulus; Panel A: for A,B stimuli; Panel B: for C,D stimuli. Gray trajectories are 5 distinct trials of the application of the odor. The starting and ending points of the plotted trajectories are 100 msec and 600 msec, respectively, after the beginning of the trial. The black bold trajectory is the averaged trajectory over the trials.

odor A and odor B respectively. Application of a single odorant ensures that the dynamical trajectory crosses only a *single* threshold line on its way to its corresponding fixed point. Experiments show that it spends only a small amount of time near the fixed point (approximately 100 msec) before returning back to the origin.

While it is difficult to measure the convergence rate of the trajectory to the fixed point, it is straightforward to detect a crossing of the threshold line. Indeed, a common hypothesis in decision making associates crossing of a threshold in neuronal activity as equivalent to making a decision [6,64]. The crossing of the threshold line in our case can be captured most effectively by computing the CRT measure, shown in Fig. 7, per each trajectory of each odorant. Results from this analysis demonstrate that after the input is introduced, the CRT curve tends toward one of the decision thresholds, passes it and then returns back to the region where no clear contrast exists between odorants. Thereby, passing of the threshold creates an evidence toward one of the odorants. Integration of such evidence over several trials can produce a significant bias towards a specific odorant. When enough crossings from trial to trial occur, strong evidence is accumulated to accurately determine an odorant.

From simulations we observe that there is a clear advantage in repetitive introduction of the input in short bursts rather than a single long input. Long input, when

noisy, creates a corresponding noisy trajectory that typically crosses the threshold line a single time and then wanders around the fixed point so that the decision is based only on one evidence. Other measures such as the time the trajectory spent near the fixed point are typically non-robust when noisy dynamics are considered. In contrast, repetitive inputs generate a mechanism that allows for better integration of evidence since for each trial it is enough to just cross the threshold once given by a simple measure like the CRT. Such a mechanism thus provides a rapid, robust approach to odor detection.

4 Discussion

The discovery that neural responses in the antennal lobe (AL), olfactory primary processing unit in insects, are encoded into spatio-temporal neural codes suggests that the dynamics of odor recognition and perception are fundamentally a low-dimensional processing phenomenon. Characterizing the dynamical mechanism responsible for such functionality is a critical step towards understanding of the neurobiological networks involved in odor perception [48]. We modeled the dynamics of the AL by developing a data-driven network model for the neural codes that appear in the recorded data from AL projection neurons. The methodology introduced

here associates a population encoding vector with each of the neural codes and derives a low-dimensional model for the dynamics of these vectors. The low-dimensional model is then used to calibrate the full computational model of the AL. Effectively, our analysis produces a high-dimensional network of neurons tuned to encode scents into low-dimensional activity patterns, i.e., the neural codes.

Comparison between the model and experiment shows strong quantitative agreement and supports the underlying theoretical concept of the dynamical dimension reduction for robust encoding. Moreover, it allows us to construct an optimal projection space for understanding odor recognition, characterize the role of lateral inhibition, and propose a scheme for the integration of evidence for dynamic decision making.

4.1 High-Dimensional Neural Network is Tuned to Exhibit Low-Dimensional Dynamics

Our primary contribution is the introduction of a new methodology that combines dimensionality reduction of dynamical systems with experimental data in order to achieve a reliable computational model, that highlights the exploitation of low-dimensional encoding in the AL. To our knowledge, this is the first successful model that combines such a data-driven methodology in conjunction with dynamical equations of FR activity.

The methodology is divided into two stages. The first stage is implicit, where we define a library of population (encoding) vectors and project the dynamic neuronal network onto these vectors [58,56]. The outcome is then restricted so that the system possesses stable orthogonal fixed points, where each orthogonal direction is associated with a different population encoding vector. This restriction determines a mapping from the high- to low-dimensional system. In the second stage of the modeling, the constructed mapping is used in conjunction with experimental recordings in order to both determine the population encoding vectors and reconstruct the AL connectome associated with each odor in the library (see Fig. 4). The construct is consistent with AL experimentally described functionality: while it is a high-dimensional neural network consisting of thousands of neurons, it appears to be tuned to exhibit low-dimensional coding dynamics.

With this theoretical framework established, we are able to suggest answers to key questions in the behavior of the AL. One of primary importance is identifying the optimal network design that maximizes contrast enhancement and reproduces the observed AL functionality. The model shows that the optimal design can be constructed by tuning the lateral-inhibition so that the

patterns of FR activity are made robust [48]. In particular, we show that asymmetric, nonlocal design of connections in a network of neurons can lead to such low dimensional robust functionality. This mechanism is distinct from the mechanisms in other sensory systems, e.g., vision, and thereby demonstrates that common wiring strategies across different sensory systems is not necessary.

Furthermore, we demonstrate that in a noisy environment, network tuning is *necessary* for robust detection of an odor, even when input keys and output codes are identical. We show that lateral-inhibition, that has been tuned, shapes the noisy input into reliable and repeatable trajectories, while inhibition that was not tuned produces noisy and unreliable trajectories. This phenomenon is experimentally observed and described as contrast enhancement. Furthermore, our work suggests that absence of lateral inhibition will result in noisier responses and scattered trajectories in the odor space. These prediction can be verified by pharmacological treatment of the AL with GABA antagonists that block inhibition.

4.2 Projection Space for Odor Detection

In previous studies, a three dimensional projection space (*odor space*) was constructed using PCA based dimension reduction. Projections of distinct odorant trajectories onto this low-dimensional space appeared to be well separated from each other [35,43]. Moreover, for each odor there was an associated fixed point that was separated from all other odor fixed points. The construction demonstrated that odorants can be classified into distinct groups and suggested that odor detection may be accomplished solely from recordings and projection onto the odor space.

The odor space is the backbone of our model as well. There are key differences, however, in the construction of our underlying odor space. Specifically, we treat the data differently by dividing the population of PNs into remainder and population encoding vectors so that we achieve a model representing the dynamics of the spatio-temporal FR patterns rather than single neurons. Such a viewpoint of the data is useful since it constructs an odor space (phase space of a dynamical system) with meaningful axes, i.e., our dimensionality reduction gives an orthogonal basis as the ideal projection space for odor encoding. Specifically, each axis corresponds to individual odorant or the remainder (Fig. 2C). As a result, the odor space provides an easy means for characterizing odor recognition since a given trajectory can be simply defined. Indeed, comparison of the trajectories in the model and the experiments, Fig. 6,

confirms that the dynamical mechanism upon which the model was constructed (stable orthogonal fixed points) is the dynamical mechanism associated with odor detection.

4.3 Decision Making as a Robust Mechanism for Odor Perception

The timescales of realistic inputs indicate that odor detection occurs relatively fast and usually requires repetitive (over several trials) exposure to the same odor [40, 31]. Some animals use sniffing or other mechanisms to achieve fast repetition of similar input into the olfactory system [44, 62, 39, 54]. Furthermore, there exists experimental evidence that shows that for a longer stimulus duration (a few seconds), initial sharp response of PNs is followed by more intermittent one [14, 41]. These results suggest that the optimal strategy for scent recognition is employed by sampling the stimulus. Our analysis suggests that indeed based on the dynamics of the AL the exposure to multiple, short-time bursts of odor can be formulated as a decision making process. More precisely, we are able to prescribe an algorithm, possibly evoked by higher centers in the brain such as the mushroom body, that polls the dynamics of the AL in order to make a decision.

Examination of the projections of iFR data produced in both theory and experiment indicates that in each short trial, the most plausible dynamical response is an excursion in odor space along a trajectory attracted toward an orthogonal fixed point. In fact, the orthogonality of the fixed points allows for an optimal separation of trajectories for different odors. Due to the short timescale of the odor burst, the trajectory does not necessarily converge to the fixed point. Rather, it only approaches its vicinity (Fig. 6 and supplementary videos). In effect, it crosses the threshold line of an odorant while staying away from crossing thresholds of other odorants, see the horizontal and vertical lines in Fig. 6 and the trajectories that cross them. Indeed, a common hypothesis in decision making is that the decision is made when neuronal activity crosses a threshold [6]. Tracking trajectories that cross decision thresholds is accomplished by defining a linear contrast measure over time as we demonstrate in Fig. 7. Repetition of the same odorant stimulus permits robustness of the algorithm. With each threshold crossing, evidence is integrated towards a specific odorant stimulus. After each trial, a probability distribution is updated until there is a high probability that supports a specific odorant stimulus. This indicates that enough evidence was integrated toward one of the odorants, and thus leads to

a decision/perception for the odor, which is followed by a behavioral response corresponding to that odorant.

The proposed algorithm is scalable and can be used for the perception of complex odors, i.e., a mixture of odorants. If the odorants in the compound are of similar significance and strength, then the trajectories in the odor space may cross several thresholds of distinct odorants each time that a stimulus is applied. Repeating the application of the same stimulus, eventually will lead to reconstruction of a uniform probability distribution indicative of the distribution of odorants in the mixture. Note that to obtain a reliable probability distribution the process may require many repetitions than in the detection of a single odorant. When the mixture includes nonequal ratios of odors, the mechanism proposed here suggests that odorants will compete with each other via lateral inhibitory connections. Population encoding vectors that correspond to more dominant odorants may inhibit other population encoding vectors strongly and suppress them. Thus the constructed probability distribution of crossing the threshold can be significantly different than the distribution of the odorants in the mixture. Simulations and experiments on complex odors are currently under investigation. Additionally, the derived model could be used in conjunction with centrifugal input into the AL to explore the strategies for learning-induced modulation [13, 22, 20]. Such modulatory effects on the encoding properties are work for future studies. The model developed here provides an efficient platform for performing such studies.

References

1. Abbott, L., Luo, S.: A step toward optimal coding in olfaction. *Nature neuroscience* **10**(11), 1342–1343 (2007)
2. Afraimovich, V.S., Zhigulin, V.P., Rabinovich, M.I.: On the origin of reproducible sequential activity in neural circuits. *CHAOS* **14**(4), 1123–9 (2004). DOI 10.1063/1.1819625
3. Bell, R.A., Joachim, F.G.: Techniques for Rearing Laboratory Colonies of Tobacco Hornworms and Pink Bollworms Lepidoptera-Sphingidae-Gelechiidae. *Annals of the Entomological Society of America* **69**(2), 365–373 (1976)
4. Bhandawat, V., Olsen, S.R., Gouwens, N.W., Schlieff, M.L., Wilson, R.I.: Sensory processing in the *Drosophila* antennal lobe increases reliability and separability of ensemble odor representations. *Nat Neurosci* **10**(11), 1474–1482 (2007)
5. Bock, D.D., Lee, W.C.A., Kerlin, A.M., Andermann, M.L., Hood, G., Wetzell, A.W., Yurgenson, S., Soucy, E.R., Kim, H.S., Reid, R.C.: Network anatomy and in vivo physiology of visual cortical neurons. *Nature* **471**(7337), 177–82 (2011). DOI 10.1038/nature09802
6. Bogacz, R., Brown, E., Moehlis, J., Holmes, P., Cohen, J.D.: The physics of optimal decision making: a formal analysis of models of performance in two-alternative

- forced-choice tasks. *Psychological review* **113**(4), 700–65 (2006). DOI 10.1037/0033-295X.113.4.700
7. Brody, C.D., Hopfield, J.J.: Simple networks for spike-timing-based computation, with application to olfactory processing. *Neuron* **37**(5), 843–52 (2003)
 8. Broome, B.M., Jayaraman, V., Laurent, G.: Encoding and decoding of overlapping odor sequences. *Neuron* **51**(4), 467–82 (2006). DOI 10.1016/j.neuron.2006.07.018
 9. Brown, E.N., Kass, R.E., Mitra, P.P.: Multiple neural spike train data analysis: state-of-the-art and future challenges. *Nat Neurosci* **7**(5), 456–461 (2004). URL <http://dx.doi.org/10.1038/nn1228>
 10. Buckley, C., Nowotny, T.: Multiscale Model of an Inhibitory Network Shows Optimal Properties near Bifurcation. *Physical Review Letters* **106**(23), 1–4 (2011). DOI 10.1103/PhysRevLett.106.238109
 11. Buckley, C.L., Nowotny, T.: Transient dynamics between displaced fixed points: an alternate nonlinear dynamical framework for olfaction. *Brain research* **1434**, 62–72 (2012). DOI 10.1016/j.brainres.2011.07.032
 12. Buzsáki, G.: Neural syntax: cell assemblies, synapse-sembles, and readers. *Neuron* **68**(3), 362–85 (2010). DOI 10.1016/j.neuron.2010.09.023
 13. Cassenaer, S., Laurent, G.: Conditional modulation of spike-timing-dependent plasticity for olfactory learning. *Nature* **482**(7383), 47–52 (2012)
 14. Christensen, T., Hildebrand, J.: Frequency coding by central olfactory neurons in the sphinx moth *Manduca sexta*. *Chemical senses* (1988)
 15. Christensen, T.a., Pawlowski, V.M., Lei, H., Hildebrand, J.G.: Multi-unit recordings reveal context-dependent modulation of synchrony in odor-specific neural ensembles. *Nature neuroscience* **3**(9), 927–31 (2000). DOI 10.1038/78840
 16. Christensen, T.A., Waldrop, B.R., Hildebrand, J.G.: Multitasking in the olfactory system: context-dependent responses to odors reveal dual GABA-regulated coding mechanisms in single olfactory projection neurons. *Journal of Neuroscience* **18**, 5999–6008 (1998)
 17. Christie, J.M., Westbrook, G.L.: Lateral excitation within the olfactory bulb. *The Journal of neuroscience : the official journal of the Society for Neuroscience* **26**(8), 2269–77 (2006). DOI 10.1523/JNEUROSCI.4791-05.2006
 18. Cleland, T.a., Linstner, C.: Computation in the olfactory system. *Chemical senses* **30**(9), 801–13 (2005). DOI 10.1093/chemse/bji072
 19. Cook, P.B., McReynolds, J.S.: Lateral inhibition in the inner retina is important for spatial tuning of ganglion cells. *Nature neuroscience* **1**(8), 714–9 (1998). DOI 10.1038/3714
 20. Dacks, A.M., Riffell, J.a., Martin, J.P., Gage, S.L., Nighorn, A.J.: Olfactory modulation by dopamine in the context of aversive learning. *Journal of neurophysiology* **108**(2), 539–50 (2012). DOI 10.1152/jn.00159.2012
 21. Egger, V., Svoboda, K., Mainen, Z.F.: Mechanisms of lateral inhibition in the olfactory bulb: efficiency and modulation of spike-evoked calcium influx into granule cells. *The Journal of neuroscience : the official journal of the Society for Neuroscience* **23**(20), 7551–8 (2003)
 22. Farooqui, T., Robinson, K., Vaessin, H., Smith, B.H.: Modulation of Early Olfactory Processing by an Otopaminergic Reinforcement Pathway in the Honeybee. *The Journal of Neuroscience* **23**(12), 5370–5380 (2003)
 23. Gajic, Z., Lelic, M.: *Modern control systems engineering*. Prentice-Hall, Europe (1996)
 24. Grant, M., Boyd, S.: CVX: Matlab Software for Disciplined Convex Programming, version 1.21. url{../..}/cvx (2011)
 25. Hansson, B.S., Anton, S.: Function and morphology of the antennal lobe: new developments. *Annual review of entomology* **45**, 203–31 (2000). DOI 10.1146/annurev.ento.45.1.203
 26. Harris, K.D.: Neural signatures of cell assembly organization. *Nature reviews. Neuroscience* **6**(5), 399–407 (2005). DOI 10.1038/nrn1669
 27. Harris, K.D., Bartho, P., Chadderton, P., Curto, C., de la Rocha, J., Hollender, L., Itskov, V., Luczak, A., Marguet, S.L., Renart, A., Sakata, S.: How do neurons work together? Lessons from auditory cortex. *Hearing Research* **271**(1-2, SI), 37–53 (2011)
 28. Hildebrand, J.G., Shepherd, G.M.: Mechanisms of olfactory discrimination: converging evidence for common principles across phyla. *Annual review of neuroscience* **20**, 595–631 (1997). DOI 10.1146/annurev.neuro.20.1.595
 29. Hopfield, J., Tank, D.: Computing with Neural Circuits: A Model. *Science* **233**, 625–633 (1986)
 30. Jbabdi, S., Behrens, T.E.J.: Specialization: the connections have it. *Nat Neurosci* **15**(2), 171–172 (2012)
 31. Koehl, M.A.R., Koseff, J.R., Crimaldi, J.P., McCay, M.G., Cooper, T., Wiley, M.B., Moore, P.A.: Lobster Sniffing: Antennule Design and Hydrodynamic Filtering of Information in an Odor Plume. *Science* **294**(5548), 1948–1951 (2001). DOI 10.1126/science.1063724
 32. Krzywinski, M., Schein, J., Birol, I., Connors, J., Gascoyne, R., Horsman, D., Jones, S.J., Marra, M.a.: Circos: an information aesthetic for comparative genomics. *Genome research* **19**(9), 1639–45 (2009). DOI 10.1101/gr.092759.109
 33. Laughlin, B.Y.S.B., Osorio, D.: Mechanisms for neural signal enhancement in the blowfly compound eye. *Journal of experimental biology* **146**, 113–146 (1989)
 34. Laurent, G.: A systems perspective on early olfactory coding. *Science* **286**(5440), 723–728 (1999)
 35. Laurent, G.: Olfactory network dynamics and the coding of multidimensional signals. *Nature Reviews Neuroscience* **3**(11), 884–895 (2002)
 36. Lei, H., Reisenman, C.E., Wilson, C.H., Gabbur, P., Hildebrand, J.G.: Spiking patterns and their functional implications in the antennal lobe of the tobacco hornworm *Manduca sexta*. *PLoS ONE* **6**(8), e23382 (2011). DOI 10.1371/journal.pone.0023382. URL <http://dx.doi.org/10.1371%2Fjournal.pone.0023382>
 37. Linstner, C., Sachse, S., Galizia, C.G.: Computational modeling suggests that response properties rather than spatial position determine connectivity between olfactory glomeruli. *Journal of neurophysiology* **93**(6), 3410–7 (2005). DOI 10.1152/jn.01285.2004
 38. Luo, S.X., Axel, R., Abbott, L.F.: Generating sparse and selective third-order responses in the olfactory system of the fly. *Proceedings of the National Academy of Sciences of the United States of America* **107**(23), 10,713–8 (2010). DOI 10.1073/pnas.1005635107
 39. Mafra-Neto, A., Carde, R.T.: Fine-scale structure of pheromone plumes modulates upwind orientation of flying moths. *Nature* **369**(6476), 142–144 (1994)
 40. Mainland, J., Sobel, N.: The sniff is part of the olfactory percept. *Chemical senses* **31**(2), 181–96 (2006). DOI 10.1093/chemse/bjj012
 41. Marion-Poll, F., Tobin, T.: Temporal coding of pheromone pulses and trains in *Manduca sexta*. *Journal of Comparative Physiology A: ...* (1992)

42. Martin, J.P., Beyerlein, A., Dacks, A.M., Reisenman, C.E., Riffell, J.a., Lei, H., Hildebrand, J.G.: The neurobiology of insect olfaction: sensory processing in a comparative context. *Progress in neurobiology* **95**(3), 427–47 (2011). DOI 10.1016/j.pneurobio.2011.09.007
43. Mazor, O., Laurent, G.: Transient dynamics versus fixed points in odor representations by locust antennal lobe projection neurons. *Neuron* **48**(4), 661–73 (2005). DOI 10.1016/j.neuron.2005.09.032
44. Mazurek, M., Roitman, J., Ditterich, J., Shadlen, M.: A Role for Neural Integrators in Perceptual Decision Making. *Cerebral Cortex* **13**(11), 1257–1269 (2003). DOI 10.1093/cercor/bhg097
45. Murils, J., Jones, C.D.: Fine-scale Structure of Odor Plumes in Relation to Insect Orientation to Distant Pheromone and Other Attractant Sources. *Physiological Entomology* **6**(1), 71–86 (1981). DOI 10.1111/j.1365-3032.1981.tb00262.x
46. Nagel, K.I., Wilson, R.I.: Biophysical mechanisms underlying olfactory receptor neuron dynamics. *Nature neuroscience* **14**(2), 208–16 (2011). DOI 10.1038/nn.2725
47. Olsen, S.R., Wilson, R.I.: Lateral presynaptic inhibition mediates gain control in an olfactory circuit. *Nature* **452**(7190), 956–60 (2008). DOI 10.1038/nature06864
48. Rabinovich, M., Huerta, R., Laurent, G.: Neuroscience. Transient dynamics for neural processing. *Science* **321**(5885), 48–50 (2008). DOI 10.1126/science.1155564
49. Rabinovich, M., Volkovskii, A., Lecanda, P., Huerta, R., Abarbanel, H.D.I., Laurent, G.: Dynamical Encoding by Networks of Competing Neuron Groups: Winnerless Competition. *Physical Review Letters* **87**(6), 87–90 (2001). DOI 10.1103/PhysRevLett.87.068102
50. Reisenman, C.E., Heinbockel, T., Hildebrand, J.G.: Inhibitory interactions among olfactory glomeruli do not necessarily reflect spatial proximity. *Journal of neurophysiology* **100**(2), 554–64 (2008). DOI 10.1152/jn.90231.2008
51. Riffell, J.a., Abrell, L., Hildebrand, J.G.: Physical processes and real-time chemical measurement of the insect olfactory environment. *Journal of chemical ecology* **34**(7), 837–53 (2008). DOI 10.1007/s10886-008-9490-7
52. Riffell, J.A., Lei, H., Abrell, L., Hildebrand, J.G.: Neural basis of a pollinators buffet: olfactory specialization and learning in *Manduca sexta*. *Science* **339**(6116), 200–204 (2013). DOI 10.1126/science.1225483. URL <http://www.sciencemag.org/content/339/6116/200.abstract>
53. Riffell, J.a., Lei, H., Christensen, T.a., Hildebrand, J.G.: Characterization and coding of behaviorally significant odor mixtures. *Current biology : CB* **19**(4), 335–40 (2009). DOI 10.1016/j.cub.2009.01.041
54. Riffell, J.a., Lei, H., Hildebrand, J.G.: Neural correlates of behavior in the moth *Manduca sexta* in response to complex odors. *Proceedings of the National Academy of Sciences of the United States of America* **106**(46), 19,219–26 (2009). DOI 10.1073/pnas.0910592106
55. Seung, H.S.: Neuroscience: Towards functional connectomics. *Nature* **471**(7337), 170–172 (2011)
56. Shlizerman, E., Schroder, K., Kutz, J.N.: Neural activity measures and their dynamics. *SIAM J. Appl. Math.* **72**(4), 1260–1291 (2012)
57. Sirovich, L.: Turbulence and the dynamics of coherent structures part i: coherent structures*. *October* **XLV**(3), 561–571 (1987)
58. Sirovich, L.: Modeling the functional organization of the visual cortex. *Physica D: Nonlinear Phenomena* **96**(1-4), 355–366 (1996). DOI 10.1016/0167-2789(96)00033-4
59. Stopfer, M., Laurent, G.: Short-term memory in olfactory network dynamics. *Nature* **402**(6762), 664–668 (1999)
60. Tumlinson, J., Brennan, M., Doolittle, R., Mitchell, E., Brabham, A., Mazomenos, B., Baumhover, A., Jackson, D.: Identification of a pheromone blend attractive to *Manduca sexta* (L.) males in a wind tunnel. *Arch Insect Biochem Physiol* **271**(1 989), 255–271 (1989)
61. Tumlinson, J., Mitchell, E., Doolittle, R., Jackson, D.: Field-Tests of Synthetic *Manduca-Sexta* Sex-Pheromone. *Journal of Chemical Ecology* **20**(3), 579–591 (1994). DOI 10.1007/BF02059599
62. Vickers, N.J., Baker, T.C.: Reiterative responses to single strands of odor promote sustained upwind flight and odor source location by moths. *Proceedings of the National Academy of Sciences* **91**(13), 5756–5760 (1994)
63. Wilson, R.I.: Neural and behavioral mechanisms of olfactory perception. *Current opinion in neurobiology* **18**(4), 408–12 (2008). DOI 10.1016/j.conb.2008.08.015
64. Wong, K.F., Wang, X.J.: A recurrent network mechanism of time integration in perceptual decisions. *Journal Of Neuroscience* **26**(4), 1314–1328 (2006). DOI 10.1523/JNEUROSCI.3733-05.2006
65. Yokoi, M., Mori, K., Nakanishi, S.: Refinement of odor molecule tuning by dendrodendritic synaptic inhibition in the olfactory bulb. *Proceedings of the National Academy of Sciences of the United States of America* **92**(8), 3371–5 (1995)